








RESEARCH ARTICLE | NOVEMBER 17 2022

Lensless polarization camera for single-shot full-Stokes imaging

Nakkyu Baek ; Yujin Lee  ; Taeyoung Kim ; Jaewoo Jung ; Seung Ah Lee  




APL Photonics 7, 116107 (2022)
<https://doi.org/10.1063/5.0120465>



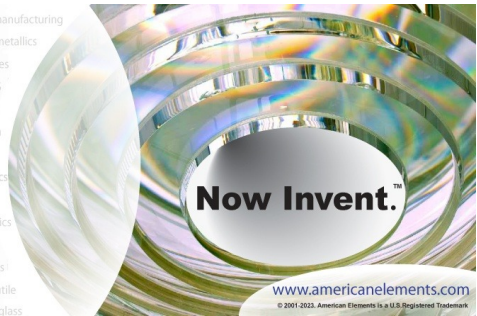
CrossMark





yttrium iron garnet, zeolites, nano ribbons, sapphire windows, spintronics, silver nanoparticles, MOCVD, rare earth metals, osmium, refractory metals, anodic aluminum oxide, niobate, ZnS, perovskite crystals, glassy carbon, ill-IV semiconductors, barium fluoride, epitaxial crystal growth, cerium oxide polishing powder, surface functionalized nanoparticles, beta-barium borate, quantum dots, scintillation Ce:YAG, laser crystals, InAs wafers, MOFs, AuNPs, CdTe, transparent ceramics, beamsplitters, gallium lump, europium phosphors, ultra high purity materials, transparent ceramics, CIGS, cermet, nanodispersions, MBE grade materials, thin film, OLED lighting, solar energy, sputtering targets, fiber optics, h-BN, deposition slugs, CVD precursors, photovoltaics, metamaterials, borosilicate glass, YBCO superconductors, InGaAs, indium tin oxide, diamond micropowder, MgF2, rutile, optical glass

additive manufacturing, organometallics, infrared dyes, transparent ceramics, CIGS, cermet, nanodispersions, MBE grade materials, thin film, OLED lighting, solar energy, sputtering targets, fiber optics, h-BN, deposition slugs, CVD precursors, photovoltaics, metamaterials, borosilicate glass, YBCO superconductors, InGaAs, indium tin oxide, diamond micropowder, MgF2, rutile, optical glass



Now Invent.™

www.americanelements.com

© 2001-2022, American Elements LLC, a U.S. Registered Trademark

The Next Generation of Material Science Catalogs

Lensless polarization camera for single-shot full-Stokes imaging

Cite as: APL Photon. 7, 116107 (2022); doi: 10.1063/5.0120465

Submitted: 12 August 2022 • Accepted: 24 October 2022 •

Published Online: 17 November 2022



View Online



Export Citation



CrossMark

Nakkyu Baek,  Yujin Lee,  Taeyoung Kim,  Jaewoo Jung,  and Seung Ah Lee^{a)} 

AFFILIATIONS

School of Electrical and Electronic Engineering, Yonsei University, Seoul 03722, Republic of Korea

^{a)} Author to whom correspondence should be addressed: seungahlee@yonsei.ac.kr

ABSTRACT

Lensless cameras have recently emerged as a compact imaging system based on computational imaging with various multiplexing capabilities. Here, we propose a compact, low-cost, lensless camera that enables snapshot full-Stokes polarization imaging. While polarization imaging provides additional contrast based on the birefringence and surface properties of the object, most polarization cameras require bulky hardware or are limited to measuring only the linear polarization information. Our device, composed of a phase mask, a polarization-encoded aperture, and a regular image sensor, performs compressed imaging to recover linear as well as circular polarization information of the scene from single image capture. We demonstrate the full-Stokes imaging capabilities of our device and describe the image reconstruction and calibration processes.

© 2022 Author(s). All article content, except where otherwise noted, is licensed under a Creative Commons Attribution (CC BY) license (<http://creativecommons.org/licenses/by/4.0/>). <https://doi.org/10.1063/5.0120465>

I. INTRODUCTION

Polarization cameras capture the polarization-dependent intensity of the scene and provide information based on the birefringence and surface properties of the object. It is widely used in various imaging applications, such as target detection and segmentation in remote sensing,¹ microscopy,² and *in vivo* imaging,³ and to measure birefringence in crystalline or photoelastic materials.^{4,5} In polarimetry, the Stokes parameters (S_0 , S_1 , S_2 , and S_3) are used to describe the amount of total intensity (S_0) and the intensities of the linear (S_1 and S_2) and circular (S_3) polarization states of the incoming light. However, many polarization imaging systems can only measure the first three (S_0 , S_1 , and S_2) components, for instance, by using commercial image sensors that have 0° , 45° , 90° , and 135° linear polarizers (LPs) patterned on each pixel.^{6–8} Circularly polarized light is utilized in many imaging or display systems to overcome the directional-dependency of the linearly polarized light, and also in specialized imaging applications, including underwater⁹ and clinical imaging.^{10,11} Thus, the ability to measure the intensity of the circularly polarized light is essential in order to implement a fully sensitive, quantitative polarimetric imaging system.¹²

For full-Stokes imaging polarimetry, at least four intensity measurements with a proper combination of linear and circular polarization channels are required. Using multiple detectors is one of the possible approaches—for example, with four cameras aligned with polarizing beam splitters¹³ or two linear-polarization cameras with and without a quarter-wave plate (QWP).¹⁴ Division-of-time methods with a rotating retarder¹⁵ or fast-switching ferroelectric liquid crystal polarizers¹⁶ on a single camera have also been demonstrated. These methods typically require multiple detectors and/or dynamic elements in the system, making the device bulky and expensive.

By contrast, a single-camera, snapshot full-Stokes polarization imaging device with a lightweight and compact form-factor can meet various polarization-sensitive imaging needs. Based on the division-of-focal-plane method, compact full-Stokes image sensors with polarization-sensitive superpixel designs have been fabricated, for example, by multiplexing a layer of LPs and another layer of retarders,^{17,18} or using a pixelated dielectric metasurface.¹⁹ Alternatively, division-of-aperture configurations remove the need for micro- to nano-optical patterning; for example, Wollaston prisms and a QWP placed in the Fourier plane of the imaging system,^{20,21} or a light-field camera with LPs and a circular polarizer (CP) embedded in front of the micro-lens array²² have successfully demonstrated

single-shot full-stokes imaging without specially fabricated detectors. Polarization-sensitive metalenses further reduce the size of the imaging system by combining the focusing optics and polarization filters into a single nano-optical component.²³ In these snapshot methods, the pixels are grouped into superpixels or the entire sensor is divided to form multiple sub-images for each polarization state, and, thus, the effective spatial resolution is reduced by the number of polarization channels. Furthermore, detectors or optical components used in these methods require specialized nanofabrication techniques, which may not be ideal for the cost-effective mass fabrication of polarization cameras.

Recently, lensless computational cameras have emerged as a compact, low-cost imaging system using light-modulating masks instead of lenses.^{24–30} Among many configurations, lensless cameras using phase-modulating masks are favored for their light collection efficiency and lower computational complexity, thanks to the shift-invariant 2D point-spread functions (PSFs). The raw measurements by the sensor are modeled using the convolution-based forward imaging model and the images of the scenes are restoration via optimization-based deconvolution processes^{29,30} or with pre-trained deep neural networks.^{31–33} Among the advantages of lensless cameras, we focus on their compressed-sensing capabilities; for instance, the depth-dependent PSFs of the weak diffuser allows for reconstructing 3D scenes from a single measurement.²⁹ Various single-shot, multiplexed imaging systems have also been demonstrated using division-of-focal plane configurations, such as high-speed imaging with rolling shutter image sensors,³⁴ hyperspectral imaging with multispectral image sensors,³⁵ and linear polarization imaging with LPs mounted on the image sensor.³⁶

In this paper, we report on a low-cost, compact, single-shot, full-Stokes polarization imaging device based on the mask-based lensless computational camera in a division-of-aperture configuration (Fig. 1). Our full-Stokes lensless polarization camera (FS-LPC)

is simply composed of a regular CMOS image sensor, a phase mask, and a polarization-encoded aperture composed of off-the-shelf LPs and a QWP and enables a snapshot full-Stokes polarimetry without any moving parts or specialized detectors. In the following sections, we describe the construction and the imaging process of the FS-LPC prototype, as well as our calibration method for the acquisition of the exact Stokes parameters of the scene. We also validate our method using polarization target objects and polarization-sensitive scenes.

II. MATERIALS AND METHODS

A. Device construction

Our lensless camera is composed of a CMOS image sensor (CIS), a phase mask, and a polarization-encoded aperture composed of three LPs and a QWP [Fig. 2(a)]. In accordance with the mask-based lensless imaging scheme,^{29,30} we use a transparent, weak-diffuser film as the phase mask, which creates a pseudo-random 2D PSF, placed in front of an image sensor. The phase mask is fabricated with polydimethylsiloxane (PDMS) elastomer by casting PDMS on a commercial diffuser (0.5° Light Shaping Diffuser Sheet, Luminit) via a simple soft-lithography process.³⁷ The casted PDMS-based phase mask does not have any birefringent properties as opposed to the commercial polycarbonate film diffusers, which may affect the polarization-dependent PSFs of the FS-LPC (see Sec. S1 of the [supplementary material](#)). Below the phase mask, we place a polarization-encoded aperture with 0°, 45°, and 90° wire-grid LP films (No. 33-084, Edmund Optics) and a right-handed circular polarizer (RHCP) made with a 45° wire-grid LP and a polymer-based QWP film (No. 88-253, Edmund Optics) with its fast-axis oriented at 0°. The polarizers and the waveplate are carefully aligned such that there is no gap between each component and the shift-invariance of the PSF is maintained [Fig. S2(b)]. The polarizer assembly is masked by a blackout aluminum tape to a square

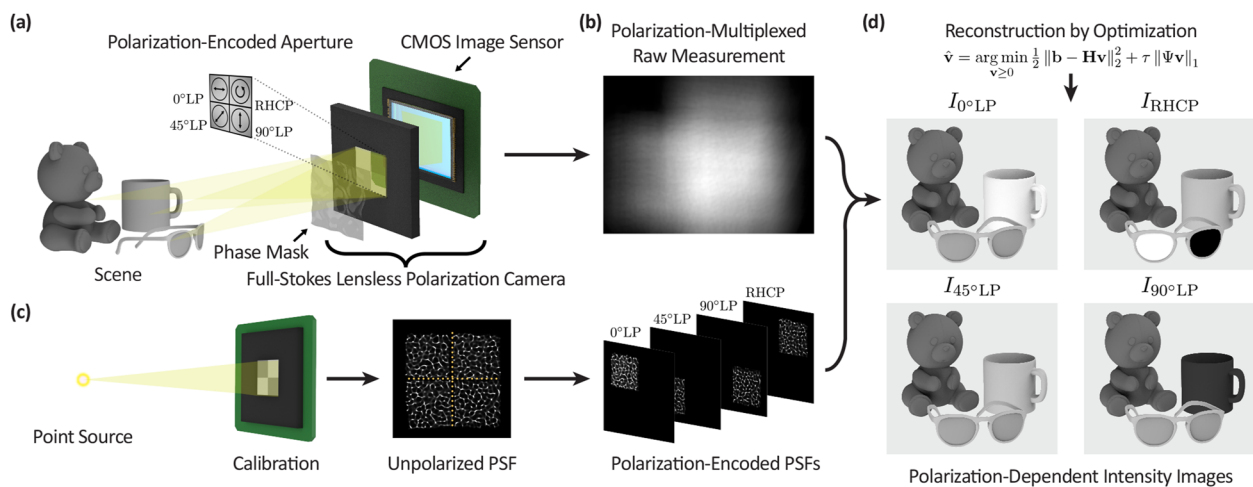


FIG. 1. (a) Overview and schematic of the full-Stokes lensless polarization camera. Light reflected from every point in the object passes through the polarization-encoded phase mask assembly in the lensless camera. (b) The captured raw image can be modeled as a summation of the 2D-convolutions between the polarization-dependent PSFs and polarization-dependent intensity of the scene. (c) The captured unpolarized PSF is divided into four channels to generate polarization-encoded PSFs in the calibration process. (d) The four polarization-dependent intensity images are reconstructed by computationally deconvolving the raw image with the PSF of the camera. Based on the four intensity images, the Stokes parameters and the other polarization parameters, including DoP, AoLP, and EA, can be calculated.

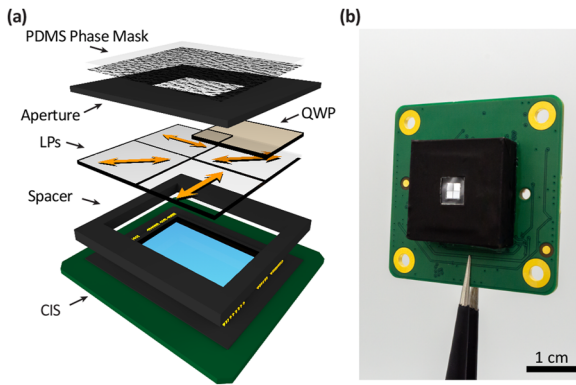


FIG. 2. (a) Configuration of the full-Stokes lensless polarization camera and (b) photograph of the prototype device.

aperture of $3 \times 3 \text{ mm}^2$ with a total thickness of $240 \mu\text{m}$. The size of the aperture is designed in consideration of the lateral field-of-view (FOV) of the camera (see [supplementary material](#) Sec. S2 for design details). Combined with the PDMS phase mask, this aperture essentially divides the phase mask into four sections and encodes each polarization light coming from the scene with distinct PSF patterns [Fig. 1(c)]. The phase mask creates a sharp, caustic PSF $\sim 6 \text{ mm}$ from the mask surface; so, we use a 3D-printed spacer to align and assemble the polarization-encoded phase mask with a commercial image sensor (IMX477, 12.3 M pixels, $1.55\text{-}\mu\text{m}$ pixel size, Sony). Figure 2(b) shows our prototype device; the effective thickness of optics is $\sim 400 \mu\text{m}$, and the total thickness of the device is 6.4 mm .

The polarization-dependent PSFs of the camera are measured prior to imaging and used in the image reconstruction process. We measured the PSF of the camera with unpolarized point source illumination (a white LED, MCWHL7, Thorlabs, with a $75 \mu\text{m}$ -pinhole) placed at the working distance (WD) of 40 cm from the camera. Then, we spatially divided the unpolarized PSF into four regions according to the position of the polarization-encoded apertures, creating a four-channel stack of polarization-dependent PSFs [Fig. 1(c)]. The measured PSFs show shift invariance in all three dimensions, within the designed lateral imaging FOV of $\sim 45^\circ$ and the axial range of the WD of $20\text{--}60 \text{ cm}$. The overall imaging FOV and the spatial resolution of the camera are evaluated experimentally (see Secs. S2 and S3 of the [supplementary material](#)). In short, the camera can image an angular FOV of $47^\circ \times 39^\circ$, and the measured two-point angular resolution, which represents the highest achievable spatial resolution in our lensless camera, is 0.135° for the same polarization and 0.105° for different (90° LP and RHCP) polarizations.

B. Image reconstruction

In lensless cameras using weak-diffuser phase masks, the imaging forward model is formulated using a simple 2D convolution between the scene and the PSF. In FS-LPC, the raw measurement captured by the image sensor can be modeled as a summation of 2D-convolutions between the PSF of each polarization channel and the intensity of the scene at the corresponding polarization. This

forward model can be expressed as $b(x, y) = \sum_j p_j(x, y) * v(x, y; j)$, where b is the sensor's measurement, p_j is the PSF of the j th polarization channel, $v(x, y; j)$ is the polarization-sensitive intensities of the scene, and $*$ denotes 2D convolution over (x, y) . Using the pre-measured PSF stack, the four polarization-dependent intensity images can be recovered from a single snapshot measurement of b . This multiplexed image reconstruction can be performed by solving the following minimization problem with the total variation regularization³⁸ and the non-negativity prior on the scene, v .

$$\hat{v} = \underset{v \geq 0}{\operatorname{argmin}} \frac{1}{2} \left\| b - \sum_j p_j * v_j \right\|_2^2 + \tau \| \Psi(v) \|_1. \quad (1)$$

Here, τ is the weight of total variation regularization in the spatial domain. Equation (1) can be solved using optimization algorithms such as alternating direction method of multipliers (ADMM).³⁹ All images are reconstructed using an ADMM-based reconstruction algorithm with fine-tuning of the total variation regularizer, and the reconstruction time for $507 \times 380 \times 4$ images is up to 24 s using Nvidia RTX3090 with Intel Xeon GOLD 6242 CPU under Ubuntu 20.04.3 LTS. After image reconstruction, the Stokes parameter images and other polarization parameters, such as degree of polarization (DoP), angle of linear polarization (AoLP), and ellipticity angle (EA), were computed to visualize the polarization information of the scene.

To test the full-Stokes imaging capabilities of our system, we made custom polarization targets where six $30 \times 30 \text{ mm}^2$ polarizing films were placed in front of bright, diffusely reflecting surfaces [Fig. 3(a)]. The targets include four LP targets designed to have 0° , 45° , 90° , and 135° LP and two CP targets with RHCP and LHCP, made with linear and circular polarizing films (No. 14-344, No. 11-047, No. 88-084, Edmund Optics). For imaging, we illuminated polarization targets with an unpolarized, white LED (MCWHL7, Thorlabs) and captured the raw image in the sensor at the WD of 40 cm , as shown in Fig. 3(b). Figure 3(c) shows reconstructed intensity images of the polarization target objects corresponding to the intensities of the targets in 0° , 45° , 90° LP and RHCP channels. According to the arrangement of the polarizers in the aperture of the lensless camera, the reconstructed pixel intensity values appear close to 1 on the target objects with the same polarization as the channel, while the objects with polarization perpendicular to the channel do not appear in the image.

To convert the recovered intensity images into Stokes parameter images, we use the following Stokes intensity formula, which represents the polarization-dependent intensity images according to the angle of the polarizer (θ) and the phase delay (ϕ) of the retarder.

$$I(\theta, \phi) = \frac{1}{2} (S_0 + S_1 \cos 2\theta + S_2 \cos \phi \sin 2\theta + S_3 \sin \phi \sin 2\theta). \quad (2)$$

Specifically, $I(\theta, \phi)$ is to represent pixel-wise intensities of the restored 2D image stack $\hat{v}(x, y; j)$ from Eq. (1). From Eq. (2), the 0° , 45° , and 90° LP , and RHCP intensities can be written as a simple, linear combination of Stokes parameters with $\theta = (0^\circ, 45^\circ, 90^\circ, \text{ and } 45^\circ)$ and $\phi = (0^\circ, 0^\circ, 0^\circ, \text{ and } 90^\circ)$, respectively. Then, we can

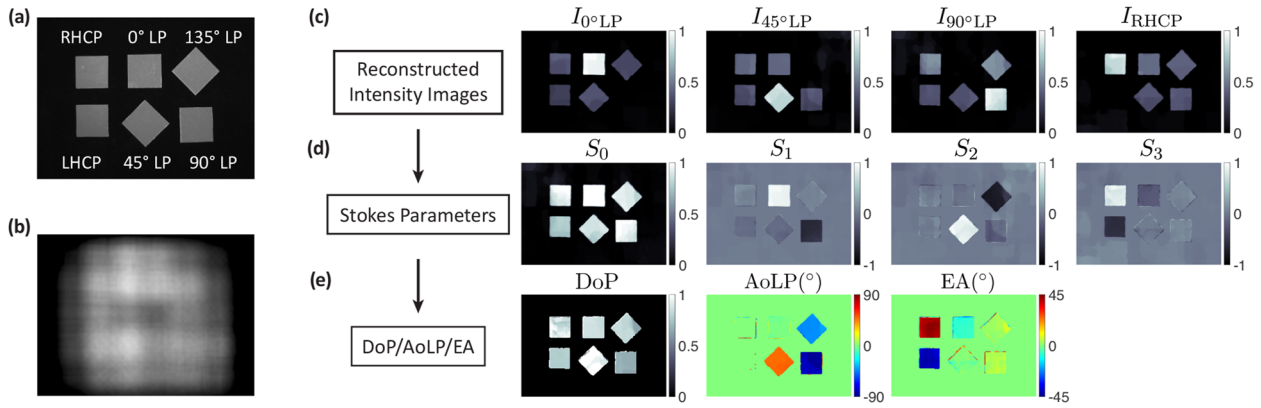


FIG. 3. Full-Stokes lensless polarization camera reconstruction process and the polarization target imaging results. (a) Polarization target objects consisted of two CPs and four LPs. (b) Raw measurement captured by FS-LPC. (c) Recovered polarization-dependent intensity images of the target objects in (a). (d) Stokes parameter images of the target objects. (e) DoP, AoLP, and EA images of the target objects.

define the ideal analysis matrix \mathbf{W} that converts the four polarized intensities, \mathbf{I} , into the Stokes vector as $\mathbf{S} = \mathbf{W}\mathbf{I}$, where

$$\mathbf{W} = \begin{bmatrix} 1 & 0 & 1 & 0 \\ 1 & 0 & -1 & 0 \\ -1 & 2 & -1 & 0 \\ -1 & 0 & -1 & 2 \end{bmatrix}. \quad (3)$$

This conversion is applied on all pixels of the images to reconstruct four Stokes parameter images as shown in Fig. 3(d). All Stokes parameter images show high-contrast values between (+1 and -1), highlighting a pair of perpendicular polarizers in each channel. Note that the Stokes parameter images reveal unwanted fluctuations in the background regions near the polarization objects that arise from the image reconstruction artifacts that cause small errors in the background regions (close to 0) of the intensity images. These reconstruction artifacts are more evident in the polarization target images because of the high contrast of the objects, and are less problematic in real-object scenes, where the polarization-dependent features are rather smooth.

From the calculated Stokes parameters, we can also compute the DoP, AoLP, and EA using the formulas below:¹²

$$\begin{aligned} \text{DoP} &= \frac{\sqrt{S_1^2 + S_2^2 + S_3^2}}{S_0}, \\ \text{AoLP} &= \frac{1}{2} \tan^{-1} \left(\frac{S_2}{S_1} \right), \\ \text{EA} &= \frac{1}{2} \sin^{-1} \left(\frac{S_3}{S_0 + \sqrt{S_1^2 + S_2^2}} \right). \end{aligned} \quad (4)$$

Specifically, DoP indicates the amount of polarization in the total reflected intensity, AoLP specifies the azimuth angle of the linear polarization, and EA indicates the degree and the direction of circular polarization. In Fig. 3(e), the DoP shows intensity close to +1 in all target objects, AoLP shows close to 45°, 90°, and -45° values,

indicating the direction of each LP, and the EA shows +45° and -45° values, indicating the handedness of the CP targets.

C. Stokes parameter calibration

The ideal analysis matrix \mathbf{W} in Eq. (3) is derived assuming that the polarizers and the wave plates mounted in the cameras are ideal, and each channel measures perfect intensity corresponding to the 0°, 45°, and 90° LP or RHCP components of the scene. However, the transmittance and the extinction coefficients of the polarizers and the wave plates are not perfect, and, thus, the analysis matrix needs to be calibrated in order to obtain the correct Stokes parameters of the scene. In the imaging process, the ground-truth Stokes vector of the scene, \mathbf{S}_{GT} , is modified by the polarizer assembly in the lensless camera to produce $\mathbf{S}_{\text{Lensless}}$, the measured Stokes vector from our lensless polarization camera. The polarization-modifying behavior of the lensless camera can be expressed in terms of a Mueller matrix of the FS-LPC, \mathbf{M} , and can be written as $\mathbf{S}_{\text{Lensless}} = \mathbf{M}\mathbf{S}_{\text{GT}}$.

Instead of measuring each element of \mathbf{M} of the polarizer assembly, we calibrated the analysis matrix directly by finding the relationship between \mathbf{S}_{GT} and $\mathbf{I}_{\text{Lensless}}$, the reconstructed intensity measurements from our FS-LPC. Subsequently, the calibrated analysis matrix \mathbf{W}' can be obtained as follows:

$$\begin{aligned} \mathbf{S}_{\text{GT}} &= \mathbf{M}^{-1} \mathbf{S}_{\text{Lensless}}, \\ &= \mathbf{M}^{-1} \mathbf{W} \mathbf{I}_{\text{Lensless}}, \\ &= \mathbf{W}' \mathbf{I}_{\text{Lensless}}. \end{aligned} \quad (5)$$

Given the lack of an ideal polarization target with known \mathbf{S}_{GT} , we calibrated our lensless polarization camera against a separate lensed full-Stokes polarization imaging system using a commercial polarization camera. A lensed polarization camera using a 5 MP monochromatic polarization image sensor (Blackfly 3, FLIR) with a C-Mount lens (TV Lens $f = 16$ mm, 1:1.4, Pentax) was used to image the scene with and without a high-performance QWP (No. 88-198, Edmund Optics) to measure what we consider as the ground-truth Stokes parameter images of the scene. \mathbf{S}_{GT} is calculated based on

the eight intensity measurements ($\theta = 0^\circ, 45^\circ, 90^\circ,$ and 135° and $\phi = 0^\circ$ and 90°) from the lensed polarization camera with an 8×4 ideal analysis matrix. At least four independent measurements of S_{GT} and $I_{Lensless}$ are required in order to fit W' from the measured values. The six-target object in Fig. 3(a) was imaged with both systems to obtain six average S_{GT} and $I_{Lensless}$ values, from which we find the calibrated analysis matrix W' as below:

$$W' = \begin{bmatrix} 1.1255 & 0.1495 & 1.0786 & -0.1516 \\ 0.9878 & -0.3806 & -0.6567 & 0.2752 \\ -0.8814 & 1.7652 & -0.8986 & 0.0747 \\ -1.1177 & -0.0769 & -0.6869 & 1.9497 \end{bmatrix}. \quad (6)$$

Compared to the ideal analysis matrix W in Eq. (3), we can identify some discrepancies in the element-wise values of the analysis matrix, caused by the non-ideal polarization properties, possible misalignment of the polarizers and the QWPs, and the cross-talk between different polarization channels in our lensless camera. However, using W' for Stokes imaging corrects for the effect of these imperfections and produces calibrated Stokes parameters close to the ground-truth values.

Using the calibrated analysis matrix, we verified the accuracy of the Stokes parameter measurements using a separate set of images of the rearranged polarization targets (Fig. 4). We compared the calibrated Stokes parameter images, as well as the polarization parameter images, against the ground truth images measured with the lensed camera. Images computed using the ideal analysis matrix [Figs. 4(a) and 4(d)] and the calibrated analysis matrix [Figs. 4(b) and 4(e)] are compared against the images taken with the ground-truth polarization camera [Figs. 4(c) and 4(f)]. After the calibration, the discrepancies between S_{GT} and $S_{Lensless}$ are reduced. For example, 135° LP and RHCP objects in the S_1 images (marked with yellow arrows in Fig. 4) are adjusted to have small positive S_1 values similar to the ground-truth Stokes parameters. S_3 values of 90° and 0° LPs (marked with green arrows in Fig. 4), as well as the EA values (black arrows in Fig. 4), also become close to the ground-truth values. As a result, the DoP, AoLP, and EA images show small adjustments, as shown in Figs. 4(d)–4(f). Overall, the root mean square error

(RMSE) between S_{GT} and $S_{Lensless}$ was reduced from 0.12 to 0.078 before and after the calibration.

It is worth noting that the Stokes parameters measured with our FS-LPC may not be perfect because S_{GT} used in the calibration process is also measured from a separate polarization imaging system, which may also contain imperfections in its own measurements. Repeating the above process with known, ideal polarization targets (if available) or calibrating our measurement against another fully-calibrated polarization imaging system can improve the accuracy of our Stokes parameters. In addition, the reconstructed image quality, as well as the accuracy of the Stokes parameters, will be dependent on the amount of noise in the measurement and the amount of regularization applied in the reconstruction. The analysis on the effect of noise and scene complexity on the Stokes parameter measurement based on image simulations can be found in Sec. S5 of the [supplementary material](#).

III. IMAGING RESULTS

To demonstrate the capability of full-Stokes imaging, we performed stress analysis of a 50-mm-diameter, plastic petri dish (Fig. 5). Injection-molded plastics show unequal stress distribution, and the disparity in the amount of stress shows different phase delays across the object. This phase delay causes the transition of polarization states and can generate additional contrast upon polarization-sensitive imaging. We placed a petri dish in front of a 135° , linearly polarized back-illumination composed of a white LED panel (Advanced Illumination) and a linear polarizer [Fig. 5(a)]. Considering the imaging FOV and the working distance range of our FS-LPC (see [supplementary material](#) Secs. S2 and S4), the petri dish was imaged at the working distance of 40 cm from the camera. After reconstruction of the intensity images, we used the calibrated analysis matrix to compute the Stokes images and the polarization parameters. For comparison, we also imaged the same object with the lensed polarization camera.

The reconstructed intensity images and the Stokes parameter images show the stress distribution in the plastic dish [Figs. 5(d) and 5(e)], and the ground-truth Stokes parameters from the lensed camera are shown for comparison [Fig. 5(f)]. Specifically, S_1 and S_2 images show stress concentrated in the top area of the dish and its

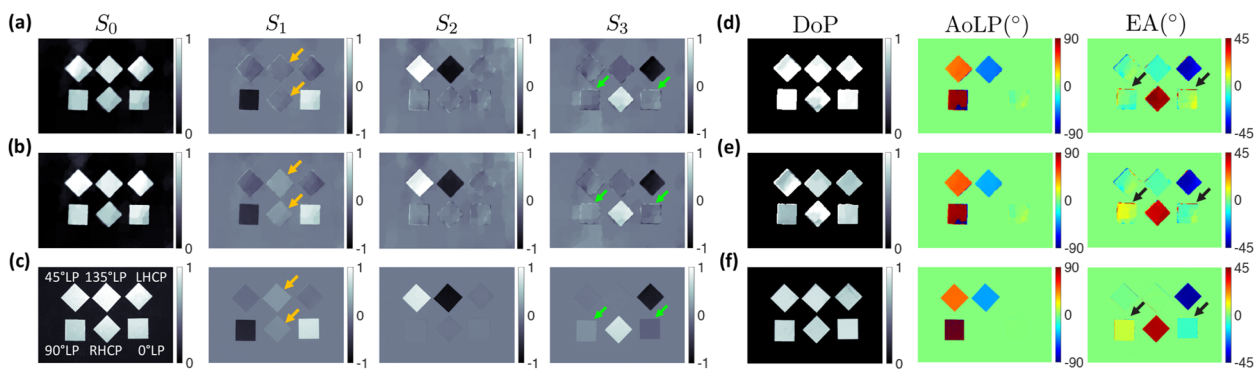


FIG. 4. Calibration of the polarization target object images. [(a)–(c)] Stokes parameters before (a) and after the calibration (b), compared against the ground-truth Stokes images (c). [(d)–(f)] DoP, AoLP, and EA images before (d) and after the calibration (e), and the ground-truth images (f).

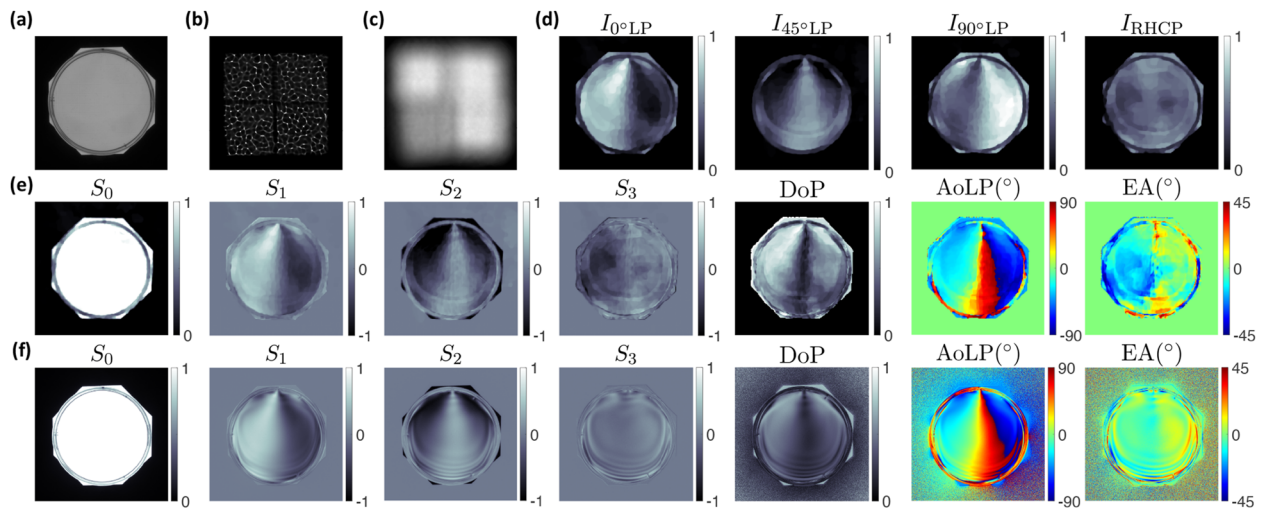


FIG. 5. Photoelasticity imaging of a polystyrene petri dish. (a) Regular photograph of the dish with 135° LP back-illumination. (b) Unpolarized 2D PSF of the camera, which is divided into four polarization-dependent PSFs for image reconstruction. (c) The raw image of the scene captured by our lensless camera. (d) Reconstructed intensity images of the object. (e) The Stokes, DoP, AoLP, and EA images from our FS-LPC. (f) The ground-truth images from the lensed polarization camera for comparison.

angular information, by the amount of change in linear polarization due to the phase delay. The 135° LP back-illumination outside the petri dish shows negative S_2 values, while S_2 and S_3 images of the dish also show some stress distributions along the rim of the dish. The calculated AoLP plot shows continuous angle transitions due to the stress distribution in the dish in lensless, as well as lensed, images [Figs. 5(e) and 5(f)]. We noticed that there is a small discrepancy in the overall baseline level of the S_3 images between our system and the ground-truth camera, which results in more significant errors in the EA images. These discrepancies suggest that while our calibrated analysis matrix W' was derived to minimize the overall error in the Stokes parameters of the polarization targets, it may not be perfect and may show more significant errors for specific polarization states.

We also captured a more complex scene consisting of multiple polarizing objects, including a stuffed animal, a pair of 3D glasses, and an LCD screen (iPad Pro 11", Apple) placed at the WD of ~ 40 cm, as shown in Fig. 6(a). We used the LCD display as the polarized back illumination for the 3D glasses, with another front-illuminating light source of a white LED (MCWHL7, Thorlabs). Figure 6(b) is the raw color measurement from our lensless polarization camera. As we use a regular, commercial color CMOS image sensor for our FS-LPC, we can reconstruct the polarization images in each color channel to form color intensity images [Fig. 6(c)], as well as color-dependent Stokes parameter images (see Sec. S7 of the supplementary material). The overall color image in Fig. 6(c) is made from S_0 images recovered from the red, green, and blue channels, showing the color of the stuffed animal and the screen. The LCD screen shows positive S_1 and negative S_3 values, indicating that the screen has left-handed elliptical polarization, with the major axis close to 0° . The measured S_3 and EA values show close to $+45^\circ$ in the RHCP lens and -45° in the LHCP lens of the 3D glasses. The stuffed animal in the scene is expected to show low DoP values, owing to the diffuse reflection of the unpolarized illumination, but the

reconstruction artifact on the lower left part of the I_{RHCP} image caused errors in the bottom half of the object.

Taking advantage of the single-shot multiplexed imaging capabilities, we can also capture the images at a video-rate of

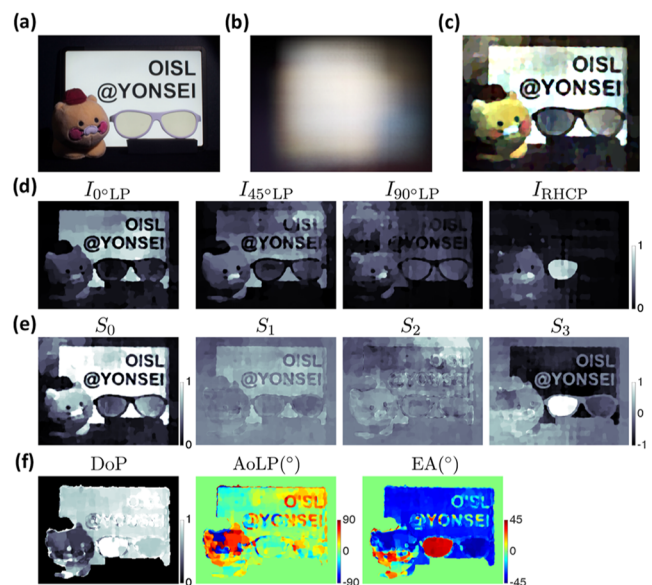


FIG. 6. (a) Regular photograph of the object composed of a doll, a pair of 3D glasses, and an LCD screen. (b) The raw measurement captured by the FS-LPC in color. (c) Reconstructed color image of the scene from S_0 images from each color channel. (d) Reconstructed polarization intensity images. (e) The Stokes parameter images from our lensless polarization camera. (f) DoP, AoLP, and EA from the lensless polarization camera.

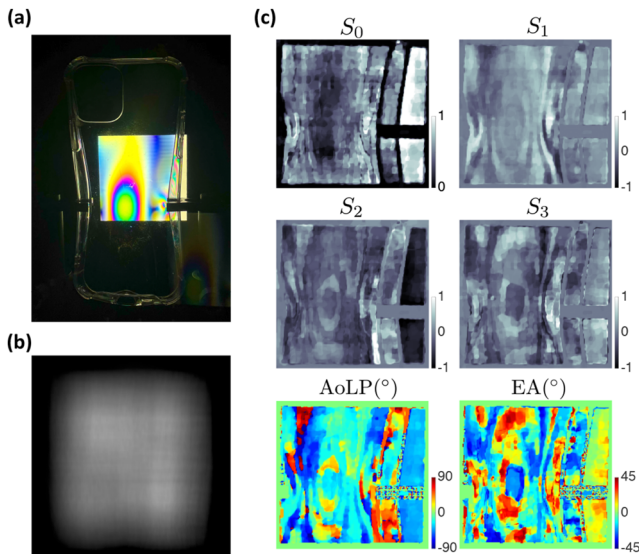


FIG. 7. (a) Photograph of experimental settings; a transparent smartphone case in front of a 135° LP back-illumination was imaged with our FS-LPC at the WD of 30 cm. (b) The raw measurement (frame No. 53) from video sequence captured by FS-LPC. (c) Stokes parameters and AoLP and EA from frame No. 53 of visualization 1.

the camera, to perform full-Stokes imaging of dynamic objects (Fig. 7). For demonstration, we imaged a transparent, thermoplastic, polyurethane smartphone case (75, 150 mm, thickness: 1.3 mm), placed in front of a 135° LP illumination, being pressed by a clamp. The polymeric films used in the smartphone case show dynamic birefringence properties under changing mechanical stress, and our FS-LPC is able to capture these changes in video-rate. For data acquisition, we captured the raw measurement for the duration of 10 s at 7 fps, which is the highest frame rate currently supported by our image sensor. Because our method uses a single measurement for four-channel images, the capturing frame rate of the raw measurements is merely determined by the frame rate of the image sensor and can exceed 30 fps by using a more advanced capture board. However, since we have not optimized our reconstruction algorithm for video processing, fast or real-time reconstruction is currently not available. The polarization-sensitive intensity images and the Stokes parameter images were reconstructed frame-by-frame after capturing the images and then were compiled into a video file (see visualization 1 in the [supplementary material](#)). For real-time, video-rate full Stokes imaging, we believe that the deep-learning-based reconstruction³³ should eventually be used instead of the iterative optimization-based reconstruction, which is slow in nature.

IV. DISCUSSION AND CONCLUSIONS

In this work, we demonstrated a mask-based, lensless polarization camera that enables single-shot full-Stokes imaging with compact, low-cost hardware. Our device captures the polarization information of a scene in a single measurement and relies on the computational image reconstruction algorithm to reconstruct the multiplexed information of the scene. The polarization-encoded

phase mask for the lensless imaging is simply constructed using the off-the-shelf components without any specialized fabrication methods, and it enables polarization-sensitive measurement with a regular, commercial CMOS image sensor. With this simple hardware configuration, we have implemented the full-Stokes imaging that can quantitatively measure the accurate Stokes parameters of the scene, as demonstrated by our polarization-target experiments and the calibration processes. We further showed the imaging performance of our device by imaging various polarization-sensitive objects and investigated the Stokes parameters and the DoP, AoLP, and EA of the scenes.

Our FS-LPC encompasses the general benefits of the lensless imaging systems in terms of cost, form factor, scalability, and the ability for compressive imaging.⁴⁰ By removing the lenses and encoding polarization information at the aperture plane, the size and cost of the polarization camera have been substantially reduced. In particular, our system utilizes low-cost off-the-shelf polarizer films and does not require any specialized detectors, such as polarization-sensitive CMOS image sensors⁷ with wire-grid polarizers deposited on each pixel. Furthermore, the entire imaging system can potentially be produced at scale using conventional semiconductor fabrication technologies. The cost-effectiveness of our FS-LPC considerably improves the possibility of using polarization imaging for object detection in a wide range of systems, including mobile devices, autonomous vehicles, and surveillance cameras. Our current device has a total track length (TTL) of 6.4 mm, which, to our knowledge, is the smallest among the reported full-Stokes imaging devices, and it can be further reduced by using a phase mask with shorter focal lengths. This is particularly advantageous with image sensors with large pixel resolutions, because TTL in lensless cameras does not depend on the size of the image sensor, as opposed to regular lensed cameras, which typically require the optics to scale with the sensor size. Furthermore, while conventional, single-shot polarization cameras using division-of-focal-plane or division-of-aperture approaches typically reduce the pixel resolution of the detector and the final optical resolution by the number of channels measured in the system, the compressive imaging capabilities⁴¹ of our FS-LPC can potentially avoid sacrificing the pixel resolution and improve the space-bandwidth product of the final images with a proper set of priors.

Despite the advantages listed above, lensless imaging is highly dependent on computational power to solve the optimization problem shown in Eq. (1), and the final quality of the images and the space-bandwidth product do not yet surpass those of lensed cameras. As the model solves an ill-posed optimization problem to reconstruct three-dimensional data from a single 2D measurement, the reconstruction is highly dependent on the SNR of the measurement, as well as the type and the amount of regularization, and the reconstruction may include unwanted artifacts that can affect the accuracy of the Stokes parameters. Additionally, imaging performance is highly dependent on the angular extent and the complexity of the scene, where the small and simple scenes tend to produce high-contrast images with less artifacts. Furthermore, the forward model used in the reconstruction process does not perfectly represent the real physical imaging processes; for example, the PSFs become shift-variant at high incident angles, and the detector is not perfectly linear. Other sources of model mismatch, such as unwanted backgrounds, stray light, or excess detector noises, can also result in

reconstruction artifacts. The total time required for reconstruction is of the order of seconds to minutes, depending on the computing resources, and will further increase with the size of the images and the complexity of the scene.

To overcome the current limitations of lensless polarization imaging, optimization of the imaging hardware, as well as a more advanced image reconstruction algorithm, is needed. The lensless camera hardware can be further improved to produce PSF patterns with low background intensity, sharp features, and high contrast, as well as more robust shift-invariant properties, to achieve higher image quality under a limited bit-depth of the detector. In addition, polarization-sensitive phase masks can be specifically designed and fabricated for lensless imaging using nanofabrication technologies. In terms of image reconstruction algorithms, the limitations of the model-based iterative algorithms are currently being addressed using deep-learning-based reconstruction methods,^{31–33,42–46} where superior image quality and faster reconstruction have been achieved for regular lensless cameras. Carefully designed reconstruction networks can consider more complex forward models, such as shift-variant PSFs,⁴⁶ or do not even require a forward model at all,³³ and, also, can utilize data-driven priors to enhance the image quality.³¹ Our FS-LPC can also utilize a designated deep-learning network for image reconstruction, trained with a combination of a simulated and experimental dataset, to effectively utilize the polarization-channel priors of the full-Stokes images of realistic scenes for specific use cases. With improved hardware and reconstruction methods, we expect that our compact lensless polarization camera can be widely used for real-time inspection and object-detection applications in various settings.

SUPPLEMENTARY MATERIAL

See the [supplementary material](#) for the birefringence analysis of the PDMS diffuser, shift invariance of PSFs, imaging performance of the FS-LPC about FOV and angular resolution, noise, and sparsity analysis, shift-invariance of PSFs at different working distances, the color-dependent Stokes parameter images, and the comparison table about recently developed, snapshot full-Stokes polarization cameras. Also, see visualization 1 for the video-rate full-Stokes imaging of the transparent, polyurethane smartphone case.

ACKNOWLEDGMENTS

This work was supported by the National Research Foundation of Korea (NRF) grant funded by the Korean government (MSIT) (Grant No. 2021R1C1C101290012).

AUTHOR DECLARATIONS

Conflict of Interest

The authors have no conflicts to disclose.

Author Contributions

Nakkyu Baek: Conceptualization (equal); Data curation (equal); Formal analysis (equal); Investigation (equal); Visualization (lead); Writing – original draft (equal); Writing – review & editing (equal).

Yujin Lee: Data curation (equal); Formal analysis (equal); Investigation (equal); Visualization (equal). **Taeyoung Kim:** Data curation (supporting); Investigation (supporting); Validation (equal). **Jaewoo Jung:** Data curation (supporting); Investigation (supporting); Validation (equal). **Seung Ah Lee:** Conceptualization (equal); Funding acquisition (lead); Investigation (equal); Project administration (lead); Supervision (lead); Writing – original draft (equal); Writing – review & editing (lead).

DATA AVAILABILITY

The data that support the findings of this study are available from the corresponding author upon reasonable request.

REFERENCES

- J. S. Tyo, D. L. Goldstein, D. B. Chenault, and J. A. Shaw, "Review of passive imaging polarimetry for remote sensing applications," *Appl. Opt.* **45**, 5453–5469 (2006).
- G. Horn, J. Lesniak, T. Mackin, and B. Boyce, "Infrared grey-field polariscope: A tool for rapid stress analysis in microelectronic materials and devices," *Rev. Sci. Instrum.* **76**, 045108 (2005).
- S. L. Jacques, J. R. Roman, and K. Lee, "Imaging superficial tissues with polarized light," *Lasers Surg. Med.* **26**, 119–129 (2000).
- Y. Zhang, S. Y. C. Lee, Y. Zhang, D. Furst, J. Fitzgerald, and A. Ozcan, "Wide-field imaging of birefringent synovial fluid crystals using lens-free polarized microscopy for gout diagnosis," *Sci. Rep.* **6**, 28793 (2016).
- K. Ramesh and S. Sasikumar, "Digital photoelasticity: Recent developments and diverse applications," *Opt. Lasers Eng.* **135**, 106186 (2020).
- M. Garcia, C. Edmiston, R. Marinov, A. Vail, and V. Gruev, "Bio-inspired color-polarization imager for real-time in situ imaging," *Optica* **4**, 1263–1271 (2017).
- Y. Maruyama, T. Terada, T. Yamazaki, Y. Uesaka, M. Nakamura, Y. Matoba, K. Komori, Y. Ohba, S. Arakawa, Y. Hirasawa *et al.*, "3.2-mp back-illuminated polarization image sensor with four-directional air-gap wire grid and 2.5- μm pixels," *IEEE Trans. Electron Devices* **65**, 2544–2551 (2018).
- M. Garcia, T. Davis, S. Blair, N. Cui, and V. Gruev, "Bioinspired polarization imager with high dynamic range," *Optica* **5**, 1240–1246 (2018).
- Y. Ding and S. Pau, "Circularly and elliptically polarized light under water and the Umov effect," *Light: Sci. Appl.* **8**, 32 (2019).
- V. V. Tuchin, "Polarized light interaction with tissues," *J. Biomed. Opt.* **21**, 071114 (2016).
- S. Sridhar and A. Da Silva, "Enhanced contrast and depth resolution in polarization imaging using elliptically polarized light," *J. Biomed. Opt.* **21**, 071107 (2016).
- D. H. Goldstein, *Polarized Light* (CRC Press, 2017).
- J. L. Pezzaniti, D. Chenault, M. Roche, J. Reinhardt, and H. Schultz, "Four camera complete Stokes imaging polarimeter," in *Polarization: Measurement, Analysis, and Remote Sensing VIII* (International Society for Optics and Photonics, 2008), Vol. 6972, p. 69720J.
- S. Shibata, M. Suzuki, N. Hagen, and Y. Otani, "Video-rate full-Stokes imaging polarimeter using two polarization cameras," *Opt. Eng.* **58**, 103103 (2019).
- S. Shibata, N. Hagen, and Y. Otani, "Robust full Stokes imaging polarimeter with dynamic calibration," *Opt. Lett.* **44**, 891–894 (2019).
- M. Vedel, S. Breugnot, and N. Lechocinski, "Full Stokes polarization imaging camera," in *Polarization Science and Remote Sensing V* (SPIE, 2011), Vol. 8160, pp. 299–311.
- X. Tu, S. McEldowney, Y. Zou, M. Smith, C. Guido, N. Brock, S. Miller, L. Jiang, and S. Pau, "Division of focal plane red–green–blue full-Stokes imaging polarimeter," *Appl. Opt.* **59**, G33–G40 (2020).
- W.-L. Hsu, G. Myhre, K. Balakrishnan, N. Brock, M. Ibn-Elhaj, and S. Pau, "Full-Stokes imaging polarimeter using an array of elliptical polarizer," *Opt. Express* **22**, 3063–3074 (2014).

- ¹⁹C. Zhang, J. Hu, Y. Dong, A. Zeng, H. Huang, and C. Wang, "High efficiency all-dielectric pixelated metasurface for near-infrared full-Stokes polarization detection," *Photonics Res.* **9**, 583–589 (2021).
- ²⁰T. Mu, C. Zhang, and R. Liang, "Demonstration of a snapshot full-Stokes division-of-aperture imaging polarimeter using Wollaston prism array," *J. Opt.* **17**, 125708 (2015).
- ²¹J. D. Perreault, "Triple Wollaston-prism complete-Stokes imaging polarimeter," *Opt. Lett.* **38**, 3874–3877 (2013).
- ²²X. Lv, S. Zhu, X. Guo, J. Zhang, J. Lin, and P. Jin, "Full-Stokes polarimetric light-field imaging using only a single detector," *Opt. Lasers Eng.* **129**, 106071 (2020).
- ²³N. A. Rubin, G. D'Aversa, P. Chevalier, Z. Shi, W. T. Chen, and F. Capasso, "Matrix Fourier optics enables a compact full-Stokes polarization camera," *Science* **365**, eaax1839 (2019).
- ²⁴M. J. DeWeert and B. P. Farm, "Lensless coded-aperture imaging with separable doubly-Toeplitz masks," *Opt. Eng.* **54**, 023102 (2015).
- ²⁵M. S. Asif, A. Ayremlou, A. Sankaranarayanan, A. Veeraraghavan, and R. G. Baraniuk, "FlatCam: Thin, lensless cameras using coded aperture and computation," *IEEE Trans. Comput. Imaging* **3**, 384–397 (2016).
- ²⁶J. K. Adams, V. Boominathan, B. W. Avants, D. G. Vercosa, F. Ye, R. G. Baraniuk, J. T. Robinson, and A. Veeraraghavan, "Single-frame 3d fluorescence microscopy with ultraminiature lensless flatscope," *Sci. Adv.* **3**, e1701548 (2017).
- ²⁷T. Shimano, Y. Nakamura, K. Tajima, M. Sao, and T. Hoshizawa, "Lensless light-field imaging with Fresnel zone aperture: Quasi-coherent coding," *Appl. Opt.* **57**, 2841–2850 (2018).
- ²⁸W. Chi and N. George, "Optical imaging with phase-coded aperture," *Opt. Express* **19**, 4294–4300 (2011).
- ²⁹N. Antipa, G. Kuo, R. Heckel, B. Mildenhall, E. Bostan, R. Ng, and L. Waller, "Diffusercam: Lensless single-exposure 3d imaging," *Optica* **5**, 1–9 (2018).
- ³⁰V. Boominathan, J. K. Adams, J. T. Robinson, and A. Veeraraghavan, "Phlatcam: Designed phase-mask based thin lensless camera," *IEEE Trans. Pattern Anal. Mach. Intell.* **42**, 1618–1629 (2020).
- ³¹S. S. Khan, V. Sundar, V. Boominathan, A. Veeraraghavan, and K. Mitra, "FlatNet: Towards photorealistic scene reconstruction from lensless measurements," *IEEE Trans. Pattern Anal. Mach. Intell.* **44**, 1934–1948 (2020).
- ³²K. Monakhova, J. Yurtsever, G. Kuo, N. Antipa, K. Yanny, and L. Waller, "Learned reconstructions for practical mask-based lensless imaging," *Opt. Express* **27**, 28075–28090 (2019).
- ³³D. Bae, J. Jung, N. Baek, and S. A. Lee, "Lensless imaging with an end-to-end deep neural network," in *2020 IEEE International Conference on Consumer Electronics-Asia (ICCE-Asia)* (IEEE, 2020), pp. 1–5.
- ³⁴N. Antipa, P. Oare, E. Bostan, R. Ng, and L. Waller, "Video from stills: Lensless imaging with rolling shutter," in *2019 IEEE International Conference on Computational Photography (ICCP)* (IEEE, 2019), pp. 1–8.
- ³⁵K. Monakhova, K. Yanny, N. Aggarwal, and L. Waller, "Spectral diffusercam: Lensless snapshot hyperspectral imaging with a spectral filter array," *Optica* **7**, 1298–1307 (2020).
- ³⁶S. Elmalem and R. Giryes, "A lensless polarization camera," in *Computational Optical Sensing and Imaging* (Optical Society of America, 2021), p. CTh7A–1.
- ³⁷Y. Lee, H. Chae, K. C. Lee, N. Baek, T. Kim, J. Jung, and S. A. Lee, "Fabrication of integrated lensless cameras via UV-imprint lithography," *IEEE Photonics J.* **14**, 1–8 (2022).
- ³⁸L. I. Rudin, S. Osher, and E. Fatemi, "Nonlinear total variation based noise removal algorithms," *Physica D* **60**, 259–268 (1992).
- ³⁹S. Boyd, N. Parikh, E. Chu, B. Peleato, J. Eckstein *et al.*, "Distributed optimization and statistical learning via the alternating direction method of multipliers," *Found. Trends Mach. Learn.* **3**, 1–122 (2011).
- ⁴⁰V. Boominathan, J. T. Robinson, L. Waller, and A. Veeraraghavan, "Recent advances in lensless imaging," *Optica* **9**, 1–16 (2022).
- ⁴¹X. Yuan, D. J. Brady, and A. K. Katsaggelos, "Snapshot compressive imaging: Theory, algorithms, and applications," *IEEE Signal Process. Mag.* **38**, 65–88 (2021).
- ⁴²J. Tan, L. Niu, J. K. Adams, V. Boominathan, J. T. Robinson, R. G. Baraniuk, and A. Veeraraghavan, "Face detection and verification using lensless cameras," *IEEE Trans. Comput. Imaging* **5**, 180–194 (2018).
- ⁴³S. S. Khan, V. Adarsh, V. Boominathan, J. Tan, A. Veeraraghavan, and K. Mitra, "Towards photorealistic reconstruction of highly multiplexed lensless images," in *Proceedings of the IEEE/CVF International Conference on Computer Vision* (IEEE, 2019), pp. 7860–7869.
- ⁴⁴J. Wu, L. Cao, and G. Barbastathis, "DNN-FZA camera: A deep learning approach toward broadband FZA lensless imaging," *Opt. Lett.* **46**, 130–133 (2021).
- ⁴⁵K. Monakhova, V. Tran, G. Kuo, and L. Waller, "Untrained networks for compressive lensless photography," *Opt. Express* **29**, 20913–20929 (2021).
- ⁴⁶K. Yanny, K. Monakhova, R. W. Shuai, and L. Waller, "Deep learning for fast spatially varying deconvolution," *Optica* **9**, 96–99 (2022).